Journal of Fluorescence, Vol. 15, No. 1, January 2005 (©2005)
DOI: 10.1007/s10895-005-0212-z

Single-Photon Counting Multicolor Multiphoton Fluorescence Microscope

Christof Buehler,[1] Ki H. Kim,[2] Urs Greuter,[1] Nick Schlumpf,[1] and Peter T. C. So[2,3,4]

Received June 17, 2004; accepted June 21, 2004

We present a multicolor multiphoton fluorescence microscope with single-photon counting sensitivity. The system integrates a standard multiphoton fluorescence microscope, an optical grating spectrograph operating in the UV–Vis wavelength region, and a 16-anode photomultiplier tube (PMT). The major technical innovation is in the development of a multichannel photon counting card (mC-PhCC) for direct signal collection from multi-anode PMTs. The electronic design of the mC-PhCC employs a high-throughput, fully-parallel, single-photon counting scheme along with a high-speed electrical or fiber-optical link interface to the data acquisition computer. There is no electronic crosstalk among the detection channels of the mC-PhCC. The collected signal remains linear up to an incident photon rate of 10^8 counts per second. The high-speed data interface offers ample bandwidth for real-time readout: 2 MByte λ-stacks composed of 16 spectral channels, 256 × 256 pixel image with 12-bit dynamic range can be transferred at 30 frames per second. The modular design of the mC-PhCC can be readily extended to accommodate PMTs of more anodes. Data acquisition from a 64-anode PMT has been verified. As a demonstration of system performance, spectrally resolved images of fluorescent latex spheres and *ex-vivo* human skin are reported. The multicolor multiphoton microscope is suitable for highly sensitive, real-time, spectrally-resolved three-dimensional imaging in biomedical applications.

KEY WORDS: Multiphoton microscopy; single-photon counting; imaging spectroscopy.

INTRODUCTION

In biology and medicine, spectroscopic measurement can be combined with optical microscopy to generate images with spatially-resolved biochemical functional information. In contrast to conventional intensity images, spectral imaging allows the quantitative determination of spectroscopic signatures of objects. Chemometric algorithm such as principal component analysis [1] can be used to analyze these spectroscopic signatures to identify concentration and spectral changes of biochemical species in the sample. Spectral imaging is commonly used to study both structures and dynamic processes in living cells [2,3]. It also opens new opportunities for the development of diagnostic tools for noninvasive tissue studies and may assist in the identification of malignant cells and the determination of surgical margin [4]. Active research in spectral imaging development reflects the scientific and clinical potential of this approach.

This paper describes the development of a spectrometer with single-photon counting sensitivity based on multi-anode photomultiplier tubes. The incorporation of the spectrometer into the multiphoton microscope is suitable for highly-sensitive, spectrally-resolved, three-dimensional imaging of cell and tissue specimens.

The accuracy of spectroscopic studies in thick specimens using conventional, one-photon, fluorescence microscopes are often susceptible to factors such as photobleaching, background fluorescence, and inner filter effects. These measurement artifacts can be avoided by using multiphoton excitation (MPE) of fluorescence. The

[1] Paul Scherrer Institut, CH-5232 Villigen, Switzerland.
[2] Department of Mechanical Engineering, Massachusetts Institute of Technology, Cambridge, Massachusetts.
[3] Biological Engineering Division, Massachusetts Institute of Technology, Cambridge, Massachusetts.
[4] To whom correspondence should be addressed at 77 Massachusetts Avenue, NE47-279, Cambridge, Massachusetts 02139.

MPE process was predicted first by Goeppert-Mayer [5]. Instead of exciting a fluorophore using a single photon of short wavelength (UV–Vis), MPE results from its simultaneous absorption of two (or more) photons typically in the infrared (IR) wavelength region. Multiphoton excitation is an ideal technique for deep tissue studies: (1) The nonlinear nature of MPE confines the fluorescence excitation volume to a sub-femtoliter region at the focal plane. Therefore, it has inherent three-dimensional resolution and reduces tissue photodamage. (2) Infrared excitation light has lower scattering and absorption coefficients in tissues, thus, allowing deeper tissue penetration. (3) Many (near) UV-excitable endogenous tissue fluorophores such as NAD(P)H, flavoproteins, collagen, and elastin can be efficiently excited via MPE using femtosecond mode-locked lasers. (4) Imaging based on MPE does not require the use of an emission pinhole for three-dimensional signal localization as in the confocal microscopy. Therefore, MPE is insensitive to emission point spread function degradation caused by scattering of emission photons in the specimen. Multiphoton excitation imaging in living tissues down to a depth of 500 micrometers has been demonstrated. Since its invention over a decade ago [6], multiphoton fluorescence microscopy has found many applications in neurobiology and embryology. Multiphoton excitation has also been used to examine tissue physiology including the cornea structure of rabbit eyes [7], the human and mouse dermal and subcutaneous structures [8–10], the metabolic processes of pancreatic islets [11,12], as well as skin lesion and wound healing processes and transdermal drug delivery [13,14].

Spectral Imaging Techniques

The design goals of a high-performance multiphoton spectral imager for deep tissue specimens are single-photon sensitivity, maximum light throughput (collection efficiency), adequate spectral resolution to distinguish chromophores (a few nanometers), and high-speed data acquisition. The components that directly affect the performance of the instrument are the spectral-resolving devices, photodetectors, and their readout electronics.

Spectrally-resolved imaging aims to record a multi-dimensional data set in which each voxel (volume-element) is defined by its spatial location (x, y, z) and its spectral signature (λ). Such a data set is often referred to as an image cube, a hyper cube, or a λ-stack (analogous to a z-stack of x–y image planes). Since photodetectors are at best two-dimensional, the acquisition of an image cube requires scanning in position and/or in wavelength. Consequently, image cubes are built progressively in two ways. (1) An image cube is generated by sequentially recording a series of two-dimensional wide field images at both different spectral bands and different depths. (2) The entire emission spectrum is acquired for a single spatial point or a line; and the image cube is then completed by sequential spatial scanning. As described subsequently each method has its unique advantages and disadvantages.

Spectral-Resolving Devices

The two approaches for image cube generation require different spectral-resolving devices: band-pass devices and spectral dispersive devices. Band-pass devices include band-pass filter wheels, or electrically tunable filters. The typical spectral dispersive devices are prisms and gratings.

Mechanical filter wheels are the most common band-pass devices. A complete spectral data set is recorded by mechanically placing filters of different pass bands into the imaging light path. The spectral resolution and transmission efficiency is determined by the filter type used. Typical efficiencies of holographic band-pass filters are approximately 70–80%. Since the filters are exchanged mechanically, the data acquisition is slow and strictly sequential in terms of wavelength scanning. Electrically tunable filters such as liquid-crystal tunable filters (LCTF), or acoustic-optical tunable filters (AOTF) are alternative band-pass devices that provide fast (micro- to milliseconds) and random switching through a sequence of wavelengths [15,16]. A typical LCTF employs a stack of polarizers and birefringent liquid crystal plates that act as voltage-tunable retarders. The transmission efficiency of LCTFs is approximately 40% across the Vis and near-IR spectral range but can drop to a few percent in the near-UV. AOTFs are solid state electro-optical devices and apply radio frequency (RF) acoustic waves in dielectric materials to diffract one (or a few) specific wavelengths of light. The performance characteristics of AOTFs is comparable to that of LCTFs, that is, AOTFs have transmission efficiencies of approximately 40% (Vis to near IR), pass bands of a few nanometers, and sub-millisecond switching speed.

Spectrally dispersive devices spread out spatially the spectral components of the incident light. Due to their higher dispersive power, gratings are used more frequently than prisms. Spectrographs are grating-based devices and provide a full spectrum at their exit ports. Commercially available gratings cover the spectral range from soft X-rays to IR. Gratings typically provide spectral resolutions well below 0.1 nm, and transmission efficiencies of more than 80% at the peak wavelength.

Since multiphoton microscopes typically generate an image by raster scanning a single excitation spot, the use of spectral dispersive device is more appropriate for this type of microscopy. Incorporating single band-pass devices in multiphoton microscopes is relatively wasteful in terms of photon collection efficiency because out-of-band photons are attenuated and discarded. In contrast, parallel spectral dispersive devices are more efficient because the entire spectrum from the excitation volume is recorded with a minimal loss of photons. Therefore, a spectrograph with holographic grating is used as spectral resolving device in our multicolor multiphoton fluorescence microscope.

Photodetectors

The selection of an appropriate photodetector is critical. Typical selection criteria are spectral range, quantum efficiency (QE), electronic noise level, readout speed, single versus array detectors, and cost. Commonly used detectors are photomultiplier tubes (PMTs), avalanche photodiodes (APDs), charge coupled device (CCD) cameras, and intensified CCDs (ICCDs). Particularly promising detectors for imaging spectroscopy in multiphoton microscopes are multichannel derivatives of standard PMTs and APDs: the multi-anode PMT and the multi-pixel APD. Table I summarizes the characteristic performance of the various detectors mentioned above.

CCD cameras have become the detectors of choice in standard spectrometers and high-speed imagers including the multifocal multiphoton imaging microsope [17]. Back-thinned CCDs can achieve QE $>$ 70% for photons in the near-UV to near-IR spectral range. Note that front-illuminated CCDs generally provide QE $\approx$30–40% and have low UV sensitivity. Due to the lack of internal gain and the presence of readout noise in the output circuitry, CCD cameras are not single-photon sensitive. Alternatively, intensified CCDs can achieve single-photon sensitivity using appropriate two-dimensional intensifier tubes (e.g. micro-channel plates) in front of the standard CCD chip. The QE is approximately 40% and limited by intensifier cathode sensitivity. The major noise sources of ICCDs are the electronic noise from the intensifier tube and the multiplicative noise from the amplification processes. ICCD cameras are relatively expensive. Recently CCDs with 'on-chip multiplication' have been available with high QE (90% in visible range) and high-speed readout speed (10 MHz). Signals are amplified before readout stage so that the effect of readout noise is eliminated. While these cameras are similar to ICCDs, these have a much higher QE. In principle, both ICCDs and CCDs with on-chip multiplication are excellent detectors for spectrally-resolved imaging applications. Unfortunately, both type of CCD systems are quite expensive.

Table I. Typical performance characteristics of four types of photodetectors: multi-anode PMT (mA-PMT), charge coupled device (CCD) cameras, intensified CCDs (ICCD), and multi-pixel avalanche photodiodes (mP-APDs)

	mA-PMT	CCD	ICCD	mP-APD
QE	~25%	~80%	~40%	~50%
λ-Range	UV–NIR	VIS–IR	UV–VIS	VIS–IR
Noise	Low	Low	High	High
Sensitivity	Single photon	Few photons	Single photon	Several photons
Speed	Fast	Slow	Slow	Fast
Cost	$,$$$.-	$$,$$$.-	$$,$$$.-	$,$$$.-

Note. QE: quantum efficiency.

PMTs are the most commonly used detectors due to their high sensitivity and relatively low costs. PMTs are single photon sensitive. The internal PMT gain is on the order of 10^6. The minimal detectable light level for PMTs is determined by their dark current which is typically at the pico- and femto-ampere level at room and cryogenic temperature, respectively. Typical PMTs have broad dynamic range and remain linear over eight orders of magnitude. The use of PMTs at high photon rate is limited by dynode loading and damage. When operated in their most sensitive spectral domain, that is, the blue/green wavelength regime, PMTs provide fairly good quantum efficiencies of 20–40%. However, for wavelengths above 600 nm, their efficiencies can drop below 1%. Traditional PMTs are single pixel devices. Multi-anode PMTs have been developed where the anode of a standard PMT is subdivided into an array of separate sensitive areas (multi-pixels). Compared with their single-anode counterparts, multi-anode PMTs show very similar performance in terms of spectral sensitivity and readout speed, but they exhibit slightly higher dark count rates and there is crosstalk (2%) between adjacent anodes according to the specification from the manufacturer. Multi-anode PMTs are single-photon sensitive. With these features, several spectral imagers have been developed based on multi-anode PMTs [18–21]. The comparison of these systems are in the next section.

For higher sensitivity detection in the Vis and NIR range, APDs with silicon-based cathodes are excellent. Throughout the visible range they have quantum efficiencies of about 70%. The drawbacks of APDs are their high cost and failure rate. In addition, commercial multi-pixel APDs cannot be manufactured with sufficiently low noise to achieve single photon sensitivity. On the basis of Table I, we conclude that multi-anode PMTs provide all the necessary performance to achieve the best balance between sensitivity, readout speed, and cost for spectrally

resolved multiphoton imaging. The current drawback of multi-anode PMTs are their lower QE of about 20%, although new multi-anode PMTs with photocathodes approaching quantum efficiencies of 40% are being developed according to the manufacturer.

Detector Readout Electronics

Readout electronics for APDs and PMTs can be classified into two categories: analog detection and pulse counting devices. The output signal from the light-exposed detectors is a sequence of current pulses generated by the incident photons. Since these current pulses have finite duration, on the order of nanoseconds, significant overlap of the current pulse occurs when the signal level is high. In this case, analog detection is appropriate and the integrated current output is measured. At low light intensity, that is, when the incident photons generate well-separated current pulses, the pulse counting method is appropriate. The number of output pulses is strictly proportional to the amount of incident light. Furthermore, the detector noise can be effectively discriminated and readout is not affected by multiplicative noise. Thus, pulse counting has advantages in terms of signal-to-noise ratio (SNR) and stability over the analog pulse-averaging approach. Recently, analog readout electronics have been developed for multi-anode PMTs and have been incorporated into multiphoton fluorescence microscopes for a broad range of biomedical applications [18–20]. However, the performance of these devices may be further optimized with the increase of detection sensitivity using single-photon counting scheme, the minimization of dead time in signal acquisition, the increase of data transfer rate to the host computer [22].

We chose to implement a single-photon-counting readout electronics for multi-anode PMTs to optimize the performance of the spectrally resolved microscope for many biomedical applications where the signal level is typically low. Using advanced high-speed electronic components (broadband GHz amplifiers, re-configurable logic), we developed a multichannel photon counting card (mC-PhCC) allowing fully parallel single-photon counting across all its channels. Rate-matching 'first-in-first-out' (FIFO) data buffers serve as temporary on-board data storage queues to account for the different clock rate of the data acquisition computer. The mC-PhCC is especially designed for efficient readout of multichannel PMTs. For each detection channel, the signal remains linear for photon rates up to 10^6 counts per second (cps). Correspondingly, the high-speed data interface provides ample bandwidth to transfer λ-stacks of 16 spectral channel, 256×256 pixel images with 12-bit dynamic range at 30 frames per second to the host computer.

The essential building blocks of the mC-PhCC are field programmable gate arrays (FPGA). These reconfigurable logic devices offer both hardware speed and software flexibility. In contrast to standard electronic components, the functionality of FPGAs is defined, and thus, modifiable, by programming. State-of-the-art manufacturing processes of FPGAs support true system-on-chip (SOC) designs, that is, the implementation of a complete electronic system on a single chip. The SOC platform can incorporate microprocessor(s), memory blocks (e.g., dual ported RAM), and various predefined I/O modules (cf. intellectual properties: IPs) that allow the FPGA to connect directly to common interfaces including PCI, USB, CAN, and most recently, high-speed serial links.

Another implementation of single-photon counting spectral-resolved imager using multi-anode PMTs has been reported [21,23]. This excellent system features spectral resolution with time-correlated single photon counting (TCSPC) circuitry. As a comparison, the TCSPC system can provide pico-second precision lifetime information to complement spectral measurement. However, since there is only a single channel of TCSPC circuit implemented, photons arriving at different spectral channel within the electronic dead time of the detection circuit are rejected. In contrast, the mC-PhCC system is fully parallelized and can detect photons arriving simultaneously at multiple spectral channels. The photon detection speed of mC-PhCC system is only limited by the dead time of each individual channels which is approximately 80 ns. The dead time can be eliminated by alternating two photon counters in each channel.

EXPERIMENTAL APPARATUS AND DESCRIPTION

Experimental Setup

The schematic of the multicolor multiphoton fluorescence microscope is shown in Fig. 1. The excitation light source is a mode-locked titanium-sapphire pulsed laser with about 100 femtosecond pulse width (Mira 900, Coherent Inc., Palo Alto, CA). The excitation wavelength (λ_{ex}) is tunable from 700 to 960 nm. Both the polarization and the power of excitation light at the specimen are controlled by a half wave plate ($\lambda/2$) and a Glan-Thomson polarizer (P). Typically, tissue imaging is conducted with an average laser power of about 3–30 mW at the sample plane. A computer-controlled galvanometric x–y scanner (6350, Cambridge Technology, Watertown, MA) deflects

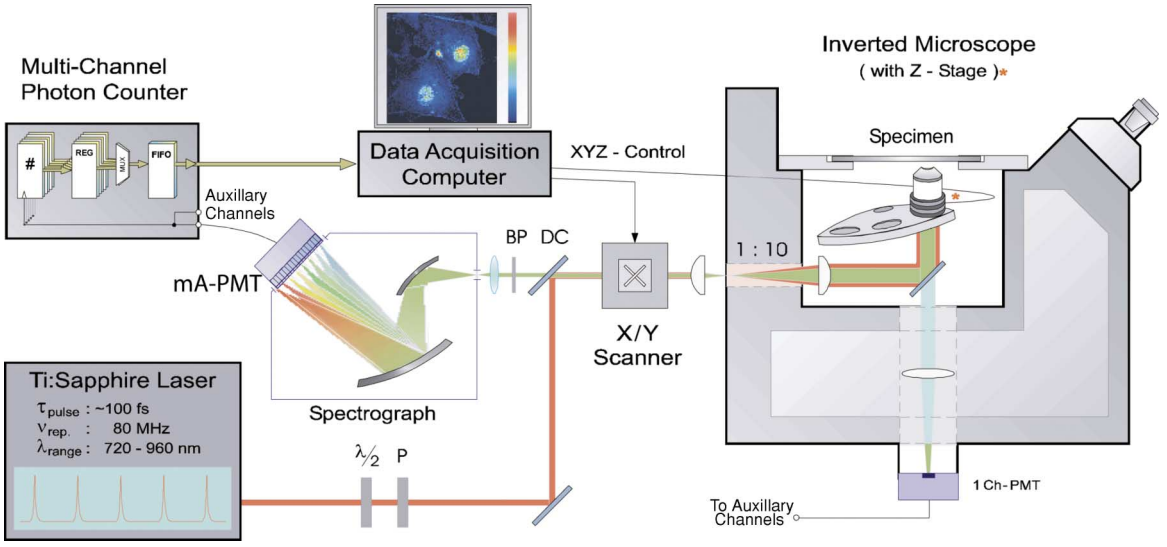

Fig. 1. Schematic diagram of the multicolor multiphoton fluorescence microscope. M = mirror; DC = dichroic mirror; BP = band-pass filter; λ/2 = half-wave plate; P = polarizer; mA-PMT = multi-anode PMT.

(raster-scans) the laser beam across the specimen. The excitation beam is coupled into an inverted microscope (Axiovert 100TV, Zeiss Inc., Thornwood, NY) via a modified epi-luminescence light path. A 1:10 beam expander ensures that the beam overfills the objective's back aperture to achieve diffraction limited focusing. Imaging at different depths is accomplished using a piezo-driven objective translator which moves the microscope objective perpendicular to imaging plane (P-721.00; Physik Instrumente, Waldbronn, Germany).

The generated fluorescence light is collected by the same objective. To ensure a spatially and angularly stationary emission beam at the entrance port of the spectrometer the fluorescence beam is de-scanned by sending it back through the microscope's excitation light path and the x–y scanner mirrors. After the scanner the emitted light passes a dichroic mirror (DC; 675DCSX, Chroma Technology Inc., Brattleboro, VT), and the residual excitation light is blocked by a barrier filter (BP; ESP650, Chroma Technology, Brattleboro, VT). The spectral dispersion of the fluorescence signal is achieved via a spectrograph (77400, ORIEL Instruments, Stratford, CT). A holographic grating (77414, ORIEL Instruments, Stratford, CT) blazed at 400 nm is used, and its efficiency is 85% at the blaze wavelength. The grating's 600 lines/mm ruling provides sub-nanometer resolution. Since it is more important to maximize the optical throughput, and since the limited number of PMT channels does not requires the full spectral resolution of the grating, the grating surface is only partially illuminated by the emission light. At the output focal plane of the spectrograph, the spectral width of emitted light spans approximately 330 nm. Its center wavelength is adjustable by rotating the grating via a micrometer. The fluorescence spectrum is detected by a 16-anode PMT (R59000U-00-L16, Hamamatsu, Bridgewater, NY), mounted onto a socket assembly with an integrated voltage divider network (E6736, Hamamatsu, Bridgewater, NY). The biasing voltage used is 800 V. Direct coupling of the PMT to the spectrograph provides a spectral resolution of 10 nm over a wavelength range of 160 nm. Higher spectral resolution can be achieved by the insertion of relay optics or the incorporation of a 32-anode PMT array (H7260, Hamamatsu, Bridgewater, NY). The 16 analog signals from the multi-anode PMT are read out by the mC-PhCC which is described in detail in the next section.

The Multichannel Photon Counting Card

Overview

The design of the multichannel photon-counting card (mC-PhCC) is shown schematically in Fig. 2. The base-module of the mC-PhCC incorporates 18 independent photon-counting channels, deep on-board buffers for short-term data storage, and two alternative high-speed interfaces to the host computer (SUB-D, GigaStar). The building blocks of the photon-counting channels are the high-speed amplifier/discriminator stages, the pulse-shaping circuitries ('one-shot'), the pulse counters (#), and their associated hold registers (REG). A set of TTL signals provide full control of the mC-PhCC, in particular, the synchronization of the data acquisition and readout

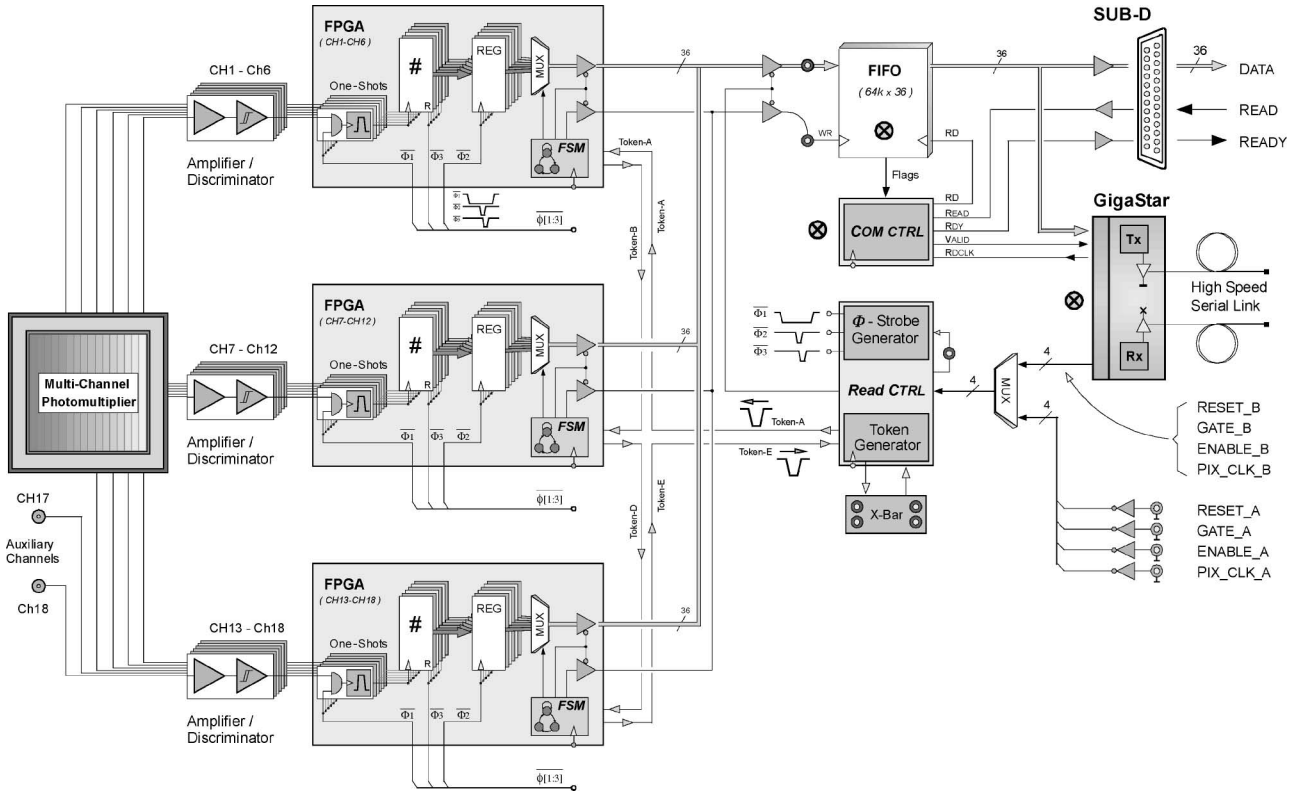

Fig. 2. Schematic diagram of the multichannel photon counter card (mC-PhCC). Photon pulse signals from the multi-anode PMT are recorded by 18 photon counting channels. Each channel comprises of amplifier/discriminator, one-shot, counter(#), and hold register (REG). Collected data are transferred to the temporary data storage (FIFO) in channel sequence and then transferred to the host computer either via a parallel link (SUB-D) or high speed serial link (GigaStar). The signals RESET, GATE, ENABLE, PIX_CLK are driven by the host computer and allow the scanner to be synchronized with the data acquisition and readout procedure of the mC-PhCC. A detailed description of the mC-PhCC is given in text.

procedure with the pixel-to-pixel movement of the scanner. Furthermore, the modular design of the mC-PhCC allows extending the number of channels for PMTs of more anodes.

Analog Circuitry

All input channels are 50 Ω terminated to minimize signal reflection. Typical photon-induced PMT signals are pulse trains with approximately 5 ns pulse duration and pulse peak voltages in the tens of mV-range. The PMT signal is preamplified by a monolithic broadband amplifier (MAR8, Mini-Circuits, Brooklyn, NY). Both the amplifier's low noise figure and its high gain (23 dB at 1 GHz) allow for precise discrimination of photon-induced pulses by a comparator with single threshold level (MAX999, Maxim Integrated Products Sunnyvale, CA). The threshold can be adjusted by a 25-turn potentiometer ($\Delta V \approx 1$ Volt). Typically, the voltage difference between the comparator's differential input pins is set to be approximately 60 mV. The duration of the discriminated photon-pulses varies significantly as a result of the PMT's broad pulse height distribution. To account for the occasionally occurring runt pulses, and their unpredicted effects on digital logic gates, each comparator output triggers a 'one-shot' pulser that generates a (well-defined) pulse of 4 ns width. The 'amplifier/discriminator/one-shot' circuitries exhibit no cross-talk and can cope with periodic pulses at rates exceeding 100 MHz. To minimize the number of components, the 'one-shot' pulsers are implemented in the FPGAs.

Digital Circuitry

The digital circuitry of the mC-PhCC is based on field-programmable gate arrays (FPGA). The actual FPGA (XCS30XL, Xilinx, San Jose, CA) has been selected primarily for its large number of global clock lines (eight), and its cost effectiveness. The global lines are low skew routing resources (<2 ns) and thus ideally suited for designing high-speed counters (#) running above 125 MHz. The dynamic range of the 18 counters is

set to 12 bit, but it can be easily adjusted (re-configured) to accommodate other experimental requirements. Typically, the measured fluorescence signal barely exceeds a few hundred photon counts per pixel (256 × 256 pixel image acquired for 7s), thus, 12-bit counters are adequate for most fluorescence applications. The design of the 18 photon counters is split into three identical FPGAs. Each FPGA comprises six 'one-shot' pulsers that drive the clock inputs of six 12-bit counters. To reduce the dead-time of the mC-PhCC, the counter values are all copied in parallel to intermediate 18-bit data registers (REG), allowing for almost immediate restart of the photon counters. The six supplementary REG-bits (high bits: 13–18) can be used for channel identification. Using three 3:1 multiplexers (MUX) REG-values are then transferred sequentially to a deep 64k × 36-bit 'first-in-first-out' data buffer (FIFO: CY7C4285V, Cypress, San Jose, CA). Since the width of the FIFO is 36-bit, the counter values plus their IDs are stored pair-wise in a channel-ascending order. The counter-to-FIFO readout procedure is fully controlled by a 40 MHz-clocked finite state machine (FSM). The data stored in the FIFO queues can be transferred to the host computer via two alternative high-speed communication interfaces: a simple, parallel link with ribbon cables for short-range (≈3 m) data transfer, and a gigabit, 'state of the art,' serial link (optical or electrical) for wide range data transfer (GigaStar, Inova Semiconductors GmbH, München, Germany).

Finite State Machine Controlled Data Readout

This section describes in detail the sequence of data readout in the mC-PhCC. Again, the mC-PhCC is fully controlled via the four TTL signals *reset*, *enable*, *gate*, and *PIX-CLK* (pixel clock). They are provided by the host computer either via separate connectors (cf. postfix '_A') or via the high-speed serial link (cf. postfix '_B'). The mC-PhCC data readout sequence is triggered by *PIX-CLK* (rising edge & *enable* = '1') and encompasses (1) immediate disabling of all counters, (2) simultaneous copying of all counter values into their individual hold registers (REG), (3) resetting and reenabling all counters, (4) transferring the REG-values to the FIFO, and (5) signaling the end of the readout sequence to the host computer by asserting data ready (RDY and VALID). Step (1) through (3) are driven via the three Φ-strobes Φ1, Φ2 and Φ3 which are generated synchronously with *PIX-CLK*. The Φ-strobe sequence requires about 30 ns to complete. Note that photon counting is inhibited only during the activity interval of the Φ-strobes. Thus, the dead-time of photon counting between successive data acquisition intervals is approximately 30 ns. The typical photon integration time between successive readouts, that is, the pixel dwell time, is on the order of 10 μs. Therefore, the duty cycle of our instrument is approximately 99.7%. Next, the data transfer from the REGs to the FIFO is mediated by means of a TOKEN (25 ns pulse width). That is, only the TOKEN-receiving FPGA is allowed to transfer its six REG-values to the FIFO. The TOKEN network connects the three FPGAs in a ring-like architecture (cf. TOKEN_A through TOKEN_E). The initial 'TOKEN_A' is generated by the readout sequence controller (Read-CTRL: XC9536XL, Xilinx, San Jose, CA) upon sensing a transition of the pixel clock (*PIX-CLK*). Upon completing its readout sequence, the FSM in the FPGA passes the TOKEN to the next FPGA (or back to the TOKEN Generator). The TOKEN mediated readout process is optimized for speed (no wait-states). The readout cycle of all 18 channels is completed within 300 ns. Moreover, the TOKEN-concept allows daisy-chaining of multiple mC-PhCC modules, thus, expanding the number of accessible PMT channels (≥128). The card-to-card routing of the TOKEN is performed via the X-bar labeled circuitry, a simple jumper-based cross-bar. Note that the figure designates electrical card-to-card connections by bold circles, and all star (⊗) designated components (e.g., FIFO, GigaStar) need to be installed only on the first mC-PhCC module. In step 5, the FIFO data is transmitted to the host computer using either of the two link interfaces. Both, the necessary link handshake signals (READ, READY) and the FIFO read-strobe (RD) are provided by the communication controller chip COM CTRL (XC9536XL, Xilinx, San Jose, CA).

For an increasing number of spectral PMT channels, the attainable performance of the mC-PhCC modules is summarized in Table II.

Table II. Data acquisition speed of the mC-PhCC electronics

PMT channels (number)	Transfer rate (parallel link) (cubes/s)	Transfer rate (serial link) [cubes/s]	Data file size (MByte/cube)
16	≤15	≤51	2.048
18	≤14	≤47	2.304
32	≤8	≤34	4.096
64	≤4	≤17	8.192
128	≤2	≤8	16.384

Note. These figures are based on transferring an image cube with spatial dimensions of 256 ×256 pixels for PMTs with various number of channels. Dynamic range of pixel data is 16 bit. The mC-PhCC supports both 36-bit parallel and high-speed serial interfaces with net transfer rates of 8 MHz and 1.2×10^9 bits per second, respectively. The data file size to be transferred is listed in the right most column.

EXPERIMENTAL RESULT AND DISCUSSION

Instrument Calibration

The discrimination levels for each photon channel are adjusted individually to maximize detection sensitivity while minimizing dark noise. At optimal threshold level, the average dark noise level is approximately 60 counts per second at room temperature which is within the specification provided by the manufacturer, and all channels have uniform sensitivity within 5% tolerance. The dark noise level is an exponential function of temperature and can be reduced significantly by detector cooling. The spectral range covered by the 16 channels was measured with a series of band-pass filters and white light illumination. For direct coupling of the spectrograph and the PMT we set the spectral range to be approximately 100 nm. The spectral band is found to be linear with channel number. The wavelength range covered by each channel is approximately 7 nm. However, the spectral range can be modified by changing the magnification of the image formed in front to the PMT via relay optics inserted between the spectrograph and the PMT. The detection efficiency of our instrument is determined mainly by that of the spectrograph and the PMT cathode. The calibration of spectral efficiency is accomplished by using a series of reference flurophores: POPOP, fluorescein, and rhodamine that jointly span the blue to near infrared spectral range. We further measured the signal loss due to additional de-scanning. Compared to the signal obtained from 'nondescanned' detectors the de-scanned signal is reduced by about 25–30%. The de-scanning losses can be reduced by anti-reflection coating of all optical component in the emission path.

Spectral Imaging of Microspheres

In order to demonstrate the spectral resolving capability of our instrument, we imaged a mixture of microspheres that differ in both sizes and spectra. Red, blue and green latex sphere with respective sizes of 1, 2, and 4 μm were used (Molecular Probes, Eugene, OR). The power of the excitation light at the specimen was 5 mW. The images were recorded by means of a Zeiss Fluar 40 $\times$ oil immersion objective with 1.25 N.A. The image size is 120 μm $\times$ 120 μm. The spectral range was tuned to span from 448 to 550 nm. Fig. 3 shows a representative three-dimensional image cube consisting of 16 two-dimensional images each at a different spectral band. The spectrally-decomposed images were recorded simultaneously (acquisition time 2.6 seconds), and no electronic cross talk has been observed between the spectral channels. As shown in Fig. 3(a) and (c), the spheres can be easily distinguished via both the size difference

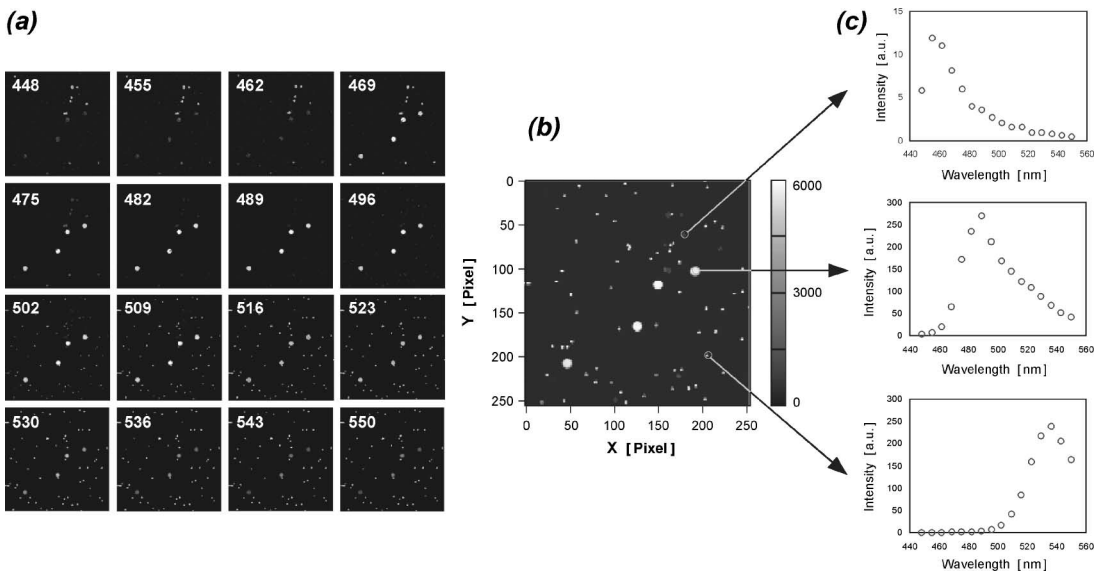

Fig. 3. Fluorescence images of *three* different color microspheres. The beads are 1, 2, and 4 μm in diameter with emission peaks at 535, 490, and 455 nm, respectively. The experimental settings are: excitation wavelength: 780 nm, power at the specimen: 5 mW, spectrum range: 100 nm, spectral resolution: 7 nm, acquisition time: 2.6 s. The color (gray level) bar represents intensity. (a) Images recorded from individual spectral channels (b) An intensity image in which signals from all 16 spectral channels are summed (c) Representative spectra of spheres: each of the three fluorescence spectra is derived from a small area around an arbitrary chosen microsphere.

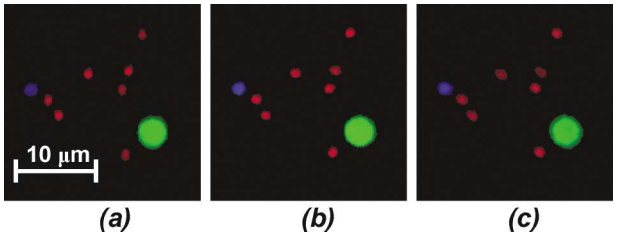

Fig. 4. High-speed three-dimensional imaging of fluorescence microspheres. Images are recorded sequentially by moving the imaging plane deeper into the sample with step size of $\Delta z = 0.5$ μm. The frame rate is 4 frame per second.

and the spectral information. The 2 μm beads appear only in the 'deep-blue' channels (cf. Fig. 3a's first 3–4 images), the 4 μm beads can be seen throughout the 'blue-green' range (middle 8–9 images), and the 1 μm beads become visible in the 'yellow-red' wavelength regime (last 6–7 images). The spectra obtained from these spheres are comparable to those obtained from standard solution fluorometry. The distinction of fluorophores with greater spectral overlap can be accomplished based on chemometric techniques [1].

High-Speed Spectral Imaging of Microspheres

Our microscope is capable to acquire spectrally resolved images at real time. To demonstrate the high-speed capability of the readout electronics we reimaged the microspheres at the maximal feasible scanning speed of *four* image planes (frames) per second. For the 256×256 pixel image the pixel residence time is 4 μs. The recorded data is transferred to the host computer via the 36-bit parallel link interface. The data transmission rate is approximately 67 Mbits per second corresponding to *four* λ-stacks each composed of 16 spectrally resolved 256 ×256 pixel images with 12-bit dynamic range. Although the maximum achievable data transmission rate can be higher, and will be limited by the internal speed of the computer, the current imaging rate is limited by the mechanical response of the galvanometric scanner used (1 KHz approximate bandwidth). Again, imaging is performed by the Zeiss Fluar 40 × oil immersion objective. Compared to the image size obtained in the slow-scanning mode (cf. Section B). Note that the actual dimension of the high-speed image is reduced to approximately 25 μm × 25 μm due to the dynamic response of the scanner. Further, the specimen was imaged dynamically during a z-scan. The recorded images were processed and individual pixels were color-labeled according to their spectra. Fig. 4 shows the time lapse sequence. The time separation between each image is 0.25 seconds, and the depth separation is approximately 0.5 μm.

Spectral Tissues Imaging

We applied our instrument to spectrally resolve structural components in *ex-vivo* tissues. The specimen studied was *ex-vivo*, previously frozen human skin (obtained from Unilever Research US, courtesy of Dr. Peter Kaplan). Skin is composed of two layers: the top layer

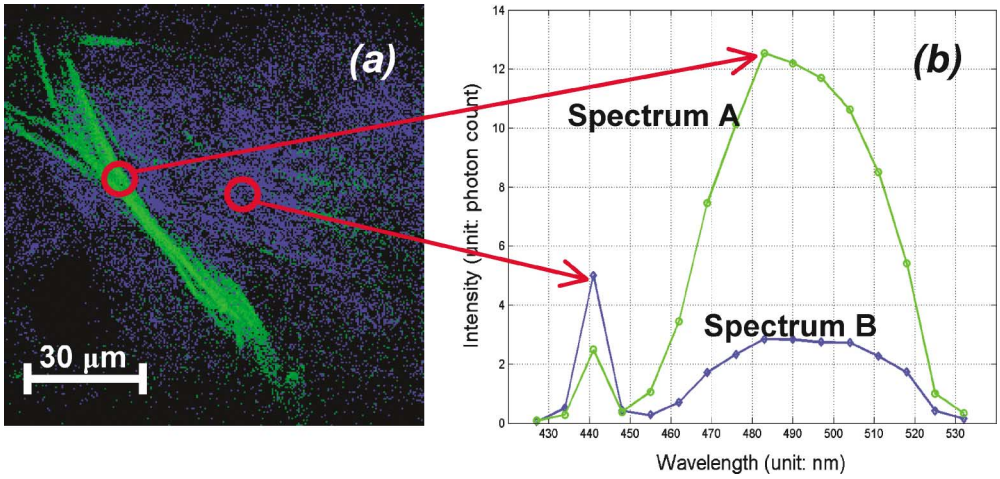

Fig. 5. Spectrally resolved imaging of *ex-vivo* human skin (dermal layer). Experimental settings are: excitation wavelength: 880 nm, power at the specimen: 5 mW, spectrum range: 100 nm, spectral resolution: 7 nm, acquisition time: 7 second per frame. (a) Color coded intensity image where blue color represents collagen and green color represents elastin (b) Representative spectra at two different positions. Position A corresponds to a collagen-rich area. Position B corresponds to an elastin rich area.

called epidermis is approximately 30–40-μm thick. The dermal layer is beneath the epidermal layer with thickness up to 1 mm. The dermal layer is composed mostly of extracellular matrix materials including collagen and elastin which are autofluorescent. At the two-photon excitation wavelength of 880 nm, the elastin fluorescence is efficiently excited but the excitation of collagen fluorescence is not optimal. However, collagen fibers are easily visualized via their second harmonic generated light [21]. The excitation light power at the specimen was 5 mW. The acquired image cube covers a spectral range from 430 to 530 nm in 7 nm intervals, with spatial dimension of 120 μm $\times$ 120 μm. The pixel residence time and the frame acquisition time were 100 μs and 7 seconds, respectively. The depth of the imaging plane was approximately 40 μm below the skin surface. A representative image is shown in Fig. 5. Both the intensity image and spectra from selected regions are shown. The intensity image is false color-labeled according to its spectrum information (channel number). All spectra obtained contain two emission peaks. The narrow emission peak at 440 nm corresponds to second harmonic generation from collagen at exactly half the excitation wavelength. The spectral width of this peak reflects the relatively narrow excitation spectrum of the Ti-Sapphire laser. The second, broader emission peak center at 490 nm corresponds to the autofluorescence of elastin. The measured spectral signature of elastin is consistent with that found in the literature [24]. On the basis of spectral decomposition, we see that the large coarse fibers corresponds to elastin-rich regions in the skin whereas the fine fibrous background corresponds to collagen-rich regions.

CONCLUSIONS

A spectrally resolved multiphoton microscope has been developed using multi-anode photomultiplier detectors operating in single photon counting mode. For high sensitivity detection using multi-anode PMTs, a dedicated multichannel photon counter card (mC-PhCC) has been developed. Single photon counting from multi-anode PMT detectors opens exciting opportunities for novel instrument development such as developing multi-focal multiphoton microscopes based on multi-anode PMTs instead of high cost CCD detectors.

ACKNOWLEDGMENTS

We acknowledge funding support from Unilever Corporation and the National Institute of Health R21/R33 CA84740-0.

REFERENCES

1. J. J. Andrew and T. M. Hancewicz (1998). Rapid analysis of Raman image data using two-way multivariate curve resolution. *Appl. Spectrosc.* **52**(6), 797–807.
2. C. Xu, W. Zipfel, J. B. Shear, R. M. Williams, and W. W. Webb (1996). Multiphoton fluorescence excitation: New spectral windows for biological nonlinear microscopy. *Proc. Natl. Acad. Sci. USA* **93**(20), 10763–10768.
3. A. Miyawaki, O. Griesbeck, R. Heim, and R. Y. Tsien (1999). Dynamic and quantitative Ca2+ measurements using improved cameleons. *Proc. Natl. Acad. Sci. USA* **96**(5), 2135–2140.
4. A. Gillenwater, R. Jacob, R. Ganeshappa, B. Kemp, A. K. El-Naggar, J. L. Palmer, G. Clayman, M. F. Mitchell, R. Richards-Kortum (1998). Noninvasive diagnosis of oral neoplasia based on fluorescence spectroscopy and native tissue autofluorescence. *Arch. Otolaryngol.* **124**(11), 1251–1258.
5. M. G. Mayer (1931). Ober Elementarakte mit zwei Quantensprungen. *Ann. der Phys.* **9**(2), 273–294.
6. W. Denk, J. H. Strickler, and W. W. Webb (1990). Two-photon laser scanning fluorescence microscopy. *Science* **248**(4951), 73–76.
7. D. W. Piston, B. R. Masters, and W. W. Webb (1995). 3-Dimensionally resolved NAD(P)H cellular metabolic redox imaging of the it-situ cornea with 2-photon excitation laser-scanning microscopy. *J. Microsc.-Oxf.* **178**, 20–27.
8. B. R. Masters, P. T. C. So, and E. Gratton (1997). Multiphoton excitation fluorescence microscopy and spectroscopy of in vivo human skin. *Biophys. J.* **72**(6), 2405–2412.
9. P. T. C. So, H. Kim, and I. E. Kochevar (1998). Two-photon deep tissue *ex-vivo* imaging of mouse dermal and subcutaneous structures. *Opt. Expr.* **3**(9), 339–350.
10. C. Buehler, K. H. Kim, C. Y. Dong, B. R. Masters, and P. T. C. So (1999). Innovations in two-photon deep tissue microscopy. *IEEE Eng. Med. Biol.* **18**(5), 23–30.
11. B. D. Bennett, T. L. Jetton, G. T. Ying, M. A. Magnuson, and D. W. Piston (1996). Quantitative subcellular imaging of glucose metabolism within intact pancreatic islets. *J. Biol. Chem.* **271**(7), 3647–3651.
12. D. W. Piston, S. M. Knobel, C. Postic, K. D. Shelton, and M. A. Magnuson (1999). Adenovirus-mediated knockout of a conditional glucokinase gene in isolated pancreatic islets reveals an essential role for proximal metabolic coupling events in glucose-stimulated insulin secretion. *J. Biol. Chem.* **274**(2), 1000–1004.
13. B. Yu, C.-Y. Dong, P. T. C. So, D. Blankschtein, and R. Langer (2001). In vitro visualization and quantification of oleic acid induced changes in transdermal transport using two-photon fluorescence microscopy. *J. Invest. Dermatol.* **117**, 16–25.
14. A. Agarwal, M. L. Coleno, V. P. Wallace, W. Y. Wu, C. H. Sun, B. J. Tromberg, and S. C. George (2002). Two-photon laser scanning microscopy of epithelial cell-modulated collagen density in engineered human lung tissue. *Tissue Eng.* **7**(2), 191–202.
15. H. R. Morris, C. C. Hoyt, P. Miller, and P. J. Treado (1996). Liquid crystal tunable filter Raman chemical imaging. *Appl. Spectrosc.* **50**(6), 805–811.
16. E. S. Wachman, W. H. Niu, and D. L. Farkas (1996). Imaging acousto-optic tunable filter with 0.35-micrometer spatial resolution. *Appl. Opt.* **35**(25), 5220–5226.
17. J. Bewersdorf, R. Pick, and S. W. Hell (1998). Multifocal multiphoton microscopy. *Opt. Lett.* **23**(9), 655–657.
18. M. E. Dickinson, W. W. Christopher, G. Bearman, R. Wolleschensky, S. Tille, and S. E. Fraser (2002). Sensitive imaging of spectrally overlapping fluorochromes using the LSM 510 META. *Proc. SPIE* **4620**, 123–136.

19. T. Haraguchi, T. Shimi, T. Koujin, N. Hashiguchi, and Y. Hiraoka (2002). Spectral imaging fluorescence microscopy. *Genes Cells* **7**, 881–887.
20. Y. L. Pan, P. Cobler, S. Rhodes, A. Potter, T. Chou, S. Holler, R. K. Chang, R. G. Pinnick, and J. P. Wolf (2001). High-speed, high-sensitivity aerosol fluorescence spectrum detection using a 32-anode photomultiplier tube detector. *Rev. Sci. Instrum.* **72**(3), 1831–1836.
21. W. Becker, A. Bergmann, C. Biskup, T. Zimmer, N. Kloecker, and K. Benndorf (2002). Multi-wavelength TCSPC lifetime imaging. *Proc. SPIE* **4620**, 79–84.
22. C. Buehler, K. H. Kim, U. Greuter, N. Schlumpf, and P. T. C. So (2002). Multicolor two-photon scanning microscopy using a 16-channel photomultiplier. *Proc. SPIE* **4620**, 217–230.
23. P. Tinnefeld, D. Herten, and M. Sauer (2001). Photophysical dynamics of single molecules studied by spectrally-resolved fluorescence lifetime imaging microscopy (SFLIM). *J. Phys. Chem. A* **105**, 7989–8003.
24. I. Freund, M. Deutsch, and A. Sprecher (1986). Connetive-tissue polarity—optical 2nd-harmonic microscopy, crossed-beam summation, and small-angle scattering in rat-tail tendon. *Biophys. J.* **50**(4), 693–712